Acta Materialia 122 (2017) 60–71

Contents lists available at ScienceDirect

Acta Materialia

journal homepage: www.elsevier.com/locate/actamat

Full length article

Competition between precipitation and dissolution in Cu–Ag alloys under high pressure torsion

B.B. Straumal [a, b, c, *], V. Pontikis [d], A.R. Kilmametov [a], A.A. Mazilkin [a, b], S.V. Dobatkin [c, e], B. Baretzky [a]

[a] Karlsruher Institut für Technologie, Institut für Nanotechnologie, 76344, Eggenstein-Leopoldshafen, Germany
[b] Institute of Solid State Physics, Russian Academy of Sciences, 142432, Chernogolovka, Russia
[c] Laboratory of Hybrid Nanomaterials, National University of Science and Technology «MISIS», Leninskii prosp. 4, 119049, Moscow, Russia
[d] Commissariat à l'Energie Atomique et aux Energies Alternatives, DEN/DANS/DMN/SRMA and DRF/IRAMIS/LSI, 91191, Gif-sur-Yvette, France
[e] A.A. Baikov Institute of Metallurgy and Materials Science, Russian Academy of Sciences, Leninskii prosp. 49, 117991, Moscow, Russia

ARTICLE INFO

Article history:
Received 26 June 2016
Received in revised form
12 September 2016
Accepted 14 September 2016

Keywords:
High-pressure torsion
Precipitation
Decomposition of solid solution
Phase transitions

ABSTRACT

Severe plastic deformation (SPD) always leads to the strong grain refinement in the materials. Logically, in two- and multiphase alloys SPD has to cause the fragmentation and dissolution of precipitates in a matrix. However, it has been observed recently, that, contrary to this generally accepted viewpoint, SPD can lead also to the decomposition of supersaturated solid solution. In this work we analyze for the first time (both experimentally and theoretically) the competition of these simultaneous processes can take place, namely (1) the dissolution of precipitates and (2) decomposition of supersaturated solid solution with precipitation of a second phase. As a result, a dynamic equilibrium between these two processes appears, and a certain steady-state concentration in a solid solution is reached.

In this work we study the high pressure torsion (HPT) of a two-phase Cu–3.9 at. % Ag alloy in two different states: (i) as-cast consisting of a (Cu) solid solution with diluted 1.9 at.% Ag and another 2 at.% Ag as fine silver precipitates and (ii) an almost homogeneous solid solution with diluted 3.9 at.% Ag obtained by homogenization at $T = 780$ °C, 900 h and subsequent water quenching. HPT at room temperature causes the partial dissolution of precipitates in the as-cast samples and partial decomposition of the solid solution in homogenized samples. After HPT, the solute concentration in the matrix is the same in both samples (about 2.9–3.0 at.% Ag). Thus, it does not depend on the initial state and is higher than the equilibrium solubility limit at the HPT temperature. This concentration is equal to solubility limit at the effective temperature of $T_{eff} \approx 680$ °C.

We also proposed the model describing the dynamic equilibrium between dissolution and precipitation in HPT. Assuming that HPT fixes the composition at matrix-precipitate interfaces, we show that HPT-enhanced diffusive transport of species is the process likely controlling the observed steady-state composition in the matrix and precipitate average diameter.

1. Introduction

Severe plastic deformation (SPD) is a family of novel methods permitting metallurgists and engineers tailoring the structure and properties of materials [1]. The idea of SPD is to deform the material in a confined space. It permits to increase the strain up to enormous values without fracture of a material. Since a material cannot break, the dynamic equilibrium between deformation-driven production of crystal defects and their relaxation (annihilation) establishes after a certain strain value. It is not astonishing that such a strong action on the material leads to various phase transformations (see Refs. [2–5] and references therein) e.g. the formation or decomposition of a supersaturated solid solution, dissolution of phases, disordering of ordered phases, amorphization of crystalline phases, synthesis of the low-temperature, high-temperature or high-pressure allotropic modifications, and nanocrystallization in the amorphous matrix.

Recently it became clear that the decomposition of (supersaturated) solid solution and dissolution of precipitates during SPD are

* Corresponding author. Karlsruher Institut für Technologie, Institut für Nanotechnologie, 76344, Eggenstein-Leopoldshafen, Germany.
E-mail address: boris.straumal@kit.edu (B.B. Straumal).

http://dx.doi.org/10.1016/j.actamat.2016.09.024
1359-6454/

not independent [6]. Moreover, the precipitation of particles of a second phase from a solid solution and their dissolution take place simultaneously and compete with each other. Due to the competition between precipitation and dissolution, a certain steady-state concentration of a second component in a solid solution is reached under SPD. The goal of this paper is to study and understand the mechanisms of this competition, both experimentally and theoretically. The Cu–Ag alloys were chosen for this purpose because all necessary structural, thermodynamic and kinetic constants are known for this well-studied system. The Cu–Ag system has also wide miscibility gap, the absence of intermediate phases and allotropic transformations which facilitates studying decomposition.

2. Experimental

The cylindrical ingots of Cu–3.9 at. % Ag alloy has been prepared by induction melting under vacuum from high purity components (5N Cu and Ag). The melt was poured in vacuum into the water-cooled cylindrical copper crucible of 10 mm diameter. The discs with diameter of $d = 10$ mm and thickness $h = 0.6$ mm have been cut from the as-cast ingots, then ground and etched in a 10% HNO_3 aqueous solution. Some samples placed in sealed and evacuated silica ampoules (residual pressure, $p = 4 \times 10^{-4}$ Pa) have been annealed at $T = 780 \pm 1$ °C during 900 h and then quenched in water at room temperature. At this composition and temperature, the alloy forms a thermodynamically stable solid solution according to the experimental phase diagram [7] (Fig. 1a, full circle). Both types of samples have been deformed by high pressure torsion (HPT) at room temperature during five anvil rotations at the rate of one rotation per minute (rpm) and under pressure, $p = 6$ GPa, in a custom built, computer-controlled device of the Bridgman anvil-type (W. Klement GmbH, Lang, Austria). The anvil with 0.2 mm groove in couple with the flat one were used to get approximately 0.35 mm of the final thickness of the samples. After HPT, the central (low-deformed) part of each disk (about 3 mm in diameter) was excluded from further investigations. Scanning electron microscopy (SEM) investigations have been carried out in a Tescan Vega TS5130 MM microscope equipped with the LINK energy-dispersive X-Ray spectrometer produced by Oxford Instruments. Transmission electron microscopy (TEM) and high resolution TEM (HREM) observations have been made by using an aberration corrected TITAN 80–300 transmission electron microscope with specimens cut from bulk samples at a 3 mm distance from the disc center and further thinned in a FEI Strata 400S dual beam facility. ACOM-TEM technique was used to recognize Cu and Ag phases in the alloys after the HPT deformation. The measurements were carried out on a Philips Tecnai F20ST operated at 200 kV in microprobe STEM mode. NanoMegas ASTAR system was used for ACOM-TEM data acquisition. A probe with about 1 nm diameter and a convergence semi-angle of 1.4 mrad was generated. A camera length of 80 mm was used to acquire the diffraction patterns [8]. X-rays diffraction (XRD) spectra have been collected with a Philips X'Pert powder diffraction apparatus operating in the Bragg–Brentano theta-two theta configuration and the Cu-K_α emission line. Parameters of the XRD peak profiles, such as peak intensity, full width at half maxima and integral breadth, were fitted by Pseudo-Voigt function. A powder LaB_6 standard provided by National Institute of Standards and Technology was used for the correction of instrumental broadening. The mean diameter of precipitates and crystallites (i.e. the size of coherent scattering domains) and micro-strain have been estimated from the broadening of diffraction peaks including reflections up to (420) via a modified Williamson–Hall method [9]. Lattice parameter evaluation was performed by Fityk software [10] using a whole profile refinement. An empirical rule known as Vegard's law was taken into account for subsequent analysis of the decomposition of solid solution or dissolution of precipitates in Cu-rich solid solutions.

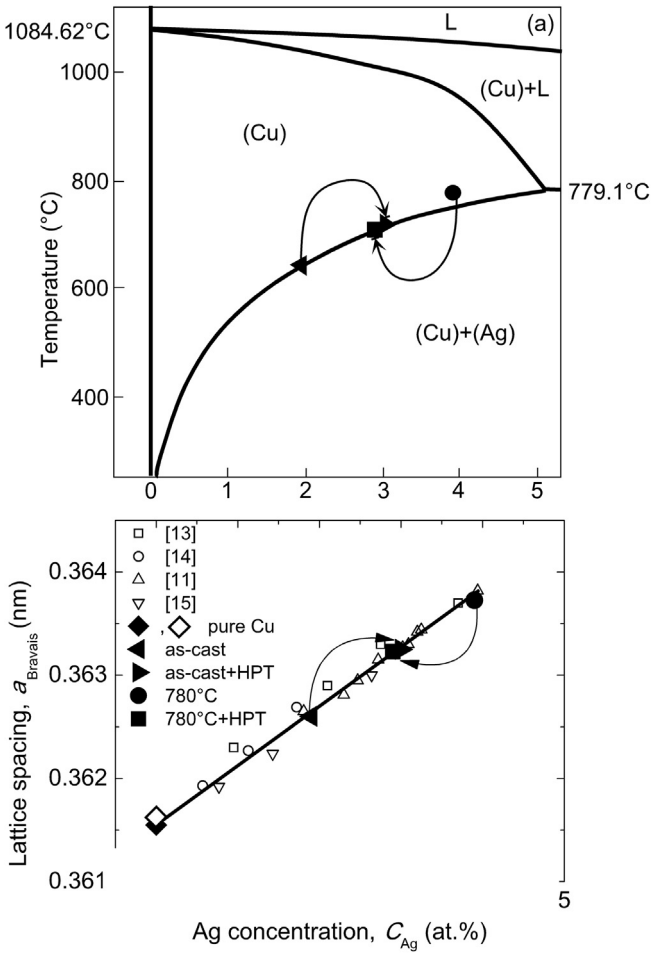

Fig. 1. (a) Cu-rich part of the Cu–Ag phase diagram drawn with data from various sources [7,11,13–15]. The nominal equilibrium composition of the alloy at $T = 780 \pm 1$ °C (full circle) equals the matrix composition of water-quenched samples after long annealing at this temperature (homogenized sample) whereas the full left-triangle marks the matrix content in Ag in the as-cast sample. Matrix compositions after HPT are shown by full right triangle for the as-cast and full square for homogenized samples. They are positioned on the solubility limit in order to show that these could be reached thermodynamically only at temperatures much larger than RT, whereas the arrows connect initial and after-HPT matrix compositions. (b) Bravais lattice constant as a function of Ag concentration in the solid solution. The full line represents the linear least-square fit through data from the literature (open symbols) [11,13–15]. Diamonds represent the lattice spacing in pure Cu: filled diamond at $T = 300$ K before HPT [15] and open diamond after HPT. Other symbols are like in Fig. 1a.

3. Experimental results

3.1. Sample microstructure before HPT

According to the XRD data, the *sample homogenized* at $T = 780 \pm 1$ °C, 900 h and quenched to room temperature (RT) contains the (Cu) solid solution with $c_n = 3.9$ at.% Ag (Fig. 1a, full circle) and vanishing small amount of silver precipitates. The matrix lattice constant determined by XRD is $a \approx 0.36365$ nm. It is close to the a value at $c_n = 3.9$ at.% Ag obtained by linearly interpolating experimental data of lattice spacing as a function of the Ag content in Cu–Ag solid solutions [11–15] (Fig. 1b, full circle). According to the SEM data, the size of (Cu) grains in homogenized

Table 1a
As-cast and homogenized samples before and after HPT. Shapes and sizes of grains/precipitates from SEM and TEM observations.

	Method	As-cast	As-cast after HPT	Homogenized	Homogenized after HPT
Diameter of precipitates or grains	SEM	Cu: 30 ± 5 μm	–	Cu: 40 ± 5 μm	–
	TEM, HREM	Ag foil-shaped: 300 × 35 nm^2	Cu: 50 ± 10 nm	Ag: e < 1 nm, D = 15 ± 7 nm	Cu: 110 ± 10 nm
		Ag spheroidal: D = 60 ± 10 nm	Ag: 20 ± 10 nm		Ag: 60 ± 10 nm

sample was about 40 μm (Table 1a). It also contained a vanishingly small volume fraction of fine Ag precipitates (Table 1b). Consistently, the XRD pattern consists of the narrow peaks of (Cu) as well as of broad and weak Ag (111) reflection. Fig. 2a shows the high resolution TEM image of a (Cu) grain in the annealed Cu–Ag sample. The grain contains tiny and homogeneously distributed Ag precipitations in the form of platelets. The platelets have a thickness of about $e \approx 0.5$ nm and are up to 30 nm in diameter D. They are precipitated coherently to the (Cu) matrix along ⟨224⟩ crystallographic directions and they lie in {111} crystallographic plane. Fig. 2b shows STEM HAADF image of such an Ag platelet. The fringes in image come from the Moiré effect of the overlapping lattice of the particle and that of the (Cu) grain. The particle looks brighter than the matrix due to the difference in Z (atomic number) of Cu and Ag. The Ag particles are coherent with the matrix and resemble the Guinier-Preston zones [16,17] encountered in aluminum-based alloys or the Co_3W zones observed in cemented carbides [18].

According to the XRD data, the *as-cast sample* consists of (Cu) solid solution with large amount of silver precipitates. XRD yields the value of the lattice constant, $a = 0.3626$ nm. Thereby the atomic fraction of Ag dissolved in the matrix has been determined via the empirical Vegard's law, $c_m \approx 1.9$ at.% Ag (Fig. 1b, full left triangle). This value corresponds to the solubility limit of a solid solution at $T \approx 680$ °C (Fig. 1a, full left triangle). Considering the above, the difference, $\delta c = c_n - c_m \approx 2$ at % Ag, does represent the precipitated Ag fraction in these samples. SEM shows that the Cu matrix is polycrystalline with grains up to 30 μm large (Table 1b). Consistently, XRD Cu peaks are narrow which also indicates that the residual lattice strains are low. The Ag precipitates are visible in TEM micrographs in bead-like shapes with average diameter of 33.8 nm (Fig. 3a and b). Few larger Ag grains ($D \approx 100$ nm) are also visible, thus weakly contributing to the width of X-ray peaks and the mean diameter of Ag grains. The quantitative evaluation of the average diameter of precipitates has also been done by XRD. Since Ag reflections up to hkl (420) are well resolved in the XRD spectra, it has been safely established that Ag precipitates are fine and almost strain free, with average diameter, $D \approx 33.4$–33.8 nm (Table 1b). Ag reflections in the alloy are slightly displaced with respect to their positions in pure Ag, the shift possibly relating to the presence of Cu atoms in solution within the precipitates. However, it has not been possible quantitatively determining the average composition of precipitates.

3.2. Sample microstructure after HPT

A feature common to deforming samples, both homogenized at $T = 780$ °C and as-cast, is that the torsion torque saturates after 1.5–2 anvil rotations, It can indicate that microstructures formed up this strain do not evolve significantly afterwards. In parallel with the torsion torque saturating, the solute concentration reaches also a stationary value of about 2.9–3.0 at.% Ag. These results resemble those obtained in recent works on Cu–Co [6] and Al–Zn [19] alloys showing that the torque and the matrix composition saturate after about 1 or 2 anvil rotations in Al-based alloys and Cu-based alloys respectively. In the following, the stationary microstructures have been characterized via three parameters, namely the amount of Ag dissolved in the Cu matrix, the average grain diameter and microstrain of the crystal lattice.

3.2.1. Ag distribution

XRD and TEM observations show that in HPT-treated samples Ag is heterogeneously distributed between precipitates and solute in the matrix. The solute fraction is different from the values determined before deformation (Tables 1a and 1b and Fig. 1a and b, full left triangles and full circles) and the solubility limit at RT. After HPT, stationary solute fractions are found practically identical in both samples (Fig. 1a and b, full right triangles and full squares). Therefore, deformation has triggered the partial decomposition of the homogenized alloy or the partial dissolution of existing precipitates in the as-cast alloy. Relying on Vegard's law (Fig. 1b), the solute fraction after HPT at RT is $c_M^h = 2.9 \pm 0.1$ at.%Ag in homogenized sample (h, full square) and c_M^{ac} at.%Ag in the as-cast sample (ac, full right triangle), respectively.

In *HPT-deformed homogenized sample*, only the first Ag(111) peak can be resolved in the XRD patterns, thereby suggesting that Ag precipitates are very tiny (Fig. 4a). Cu grains are indicated by green and Ag grains are indicated by red color in the ACOM-TEM phase maps overlaid with grain boundaries and reliability index (Fig. 4a). TEM SAED (Fig. 4c) also proves the presence of the Ag precipitates in the structure. The plot in Fig. 4c represents the results of the SAED pattern digitizing. Intensity maxima for (111), (220) and (311) Ag reflections are observed.

The XRD Ag(111) peak is slightly shifted by $\Delta\theta \approx 0.035°$ toward higher diffraction angles from its position in pure Ag. It corresponds to the 0.001 nm decrease of Ag (111) interplanar distance. The shift can be explained by the fact that Ag precipitates contain a certain

Table 1b
As-cast and homogenized samples before and after HPT. Average values of the concentration of Ag in solution (at. %), the diameter of grains/precipitates, the lattice strain and the angular width of the Ag(111) X-ray reflection. The Ag content in the matrix has been obtained via Vegard's law (Fig. 1b) by using XRD lattice constant values. Labels "F" and "B" stand for the full width at half maximum (FWHM) and for the integral peak broadening respectively.

	Method	As-cast	As-cast after HPT	Homogenized	Homogenized after HPT
Ag solute in Cu (at %)	XRD (Vegard law)	1.9 ± 0.05	3.0 ± 0.1	3.9 ± 0.05	2.9 ± 0.1
Diameter of precipitates or grains	XRD-F	Ag: 33.8 ± 1 nm	Cu: 19.3 ± 1 nm	Ag: 10 ± 2 nm	Cu: 25.1 ± 1 nm
	XRD-B	Ag: 33.4 ± 1 nm	Cu: 12.9 ± 1 nm	–	Cu: 24.6 ± 1 nm
			Ag: 12 ± 3 nm		Ag: 33.0 ± 1 nm
Lattice strain (%)	XRD-F	Ag: 0.075 ± 0.01	Cu: 0.39 ± 0.02	–	Cu: 0.25 ± 0.02
	XRD-B	Ag: 0.11 ± 0.02	Cu: 0.38 ± 0.02	–	Cu: 0.35 ± 0.02
Width of Ag-(111) peak (deg.)	XRD-F	0.235 ± 0.005	0.329 ± 0.005	–	0.248 ± 0.005
	XRD-B	0.310 ± 0.005	0.436 ± 0.005	–	0.327 ± 0.005

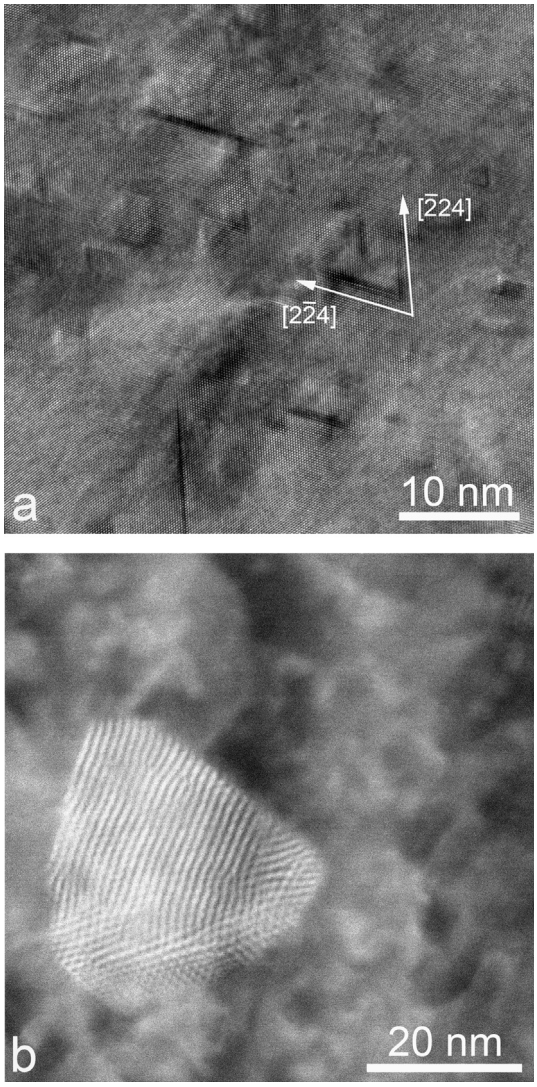

Fig. 2. HREM (a) and STEM HAADF (b) micrographs of sample annealed at $T = 780 \pm 1$ °C, 900 h before HPT.

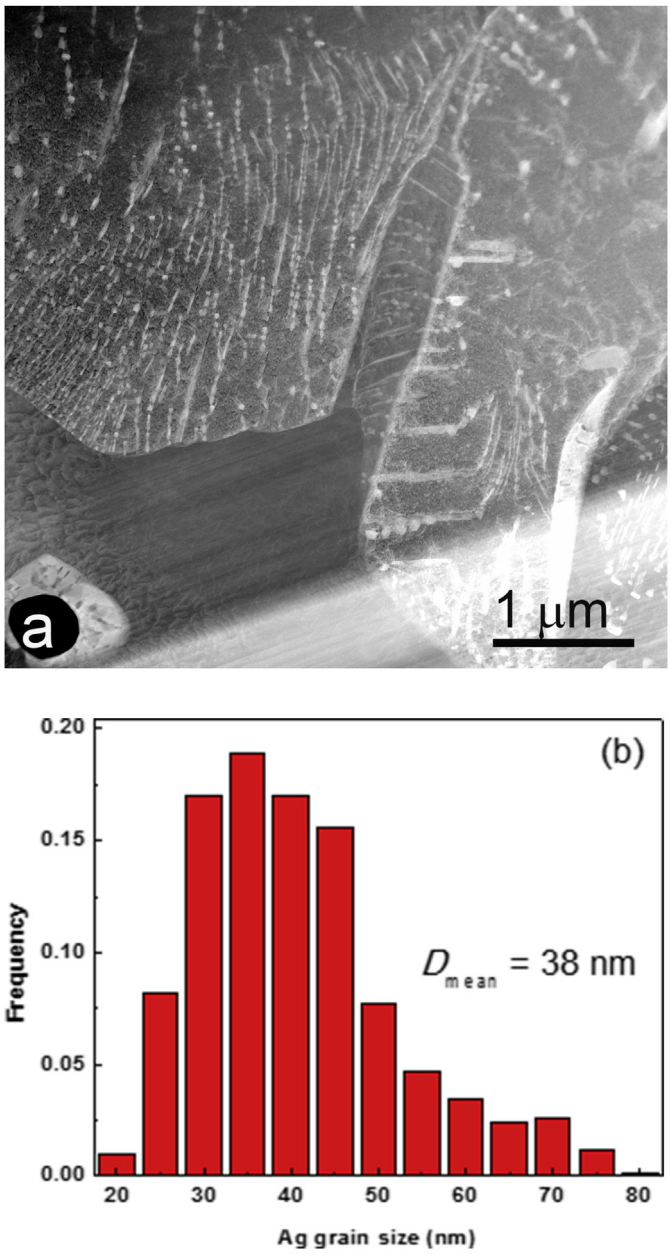

Fig. 3. (a) STEM HAADF micrograph of as-cast sample before HPT. Bright-contrast particles are equiaxed Ag precipitates either isolated or organized in long chains. Few, elongated and much larger grains ($D \geq 100$ nm) are also present. (b) Histogram of the distribution of precipitate diameters.

amount of Cu. However, the capillary force could also result in compressive strain and concomitant shift of the Ag(111) peak to higher diffraction angles. The capillary pressure can be estimated as $p = 2\sigma/r$ [20], where σ is the energy of Cu/Ag interphase boundary and $r \approx 16$ nm (Table 1b) is the radius of silver precipitates. σ for coherent interphase boundaries is about $\sigma = 75$ mJ/m^2 and for incoherent ones is $\sigma = 200–500$ mJ/m^2 [20]. The value of $\sigma = 75$ mJ/m^2 is close to the stacking fault (or symmetric twin GBs) energy in copper and the value of $\sigma = 500$ mJ/m^2 is close to the energy of asymmetric twin GBs or general GBs in copper [21–23]. TEM results (Fig. 4) witness that the Cu/Ag interphase boundaries are incoherent. It gives us the value of capillary pressure $p \approx 0.06$ GPa for $\sigma = 500$ mJ/m^2 and $r \approx 16$ nm. The distance between (111) planes in silver decreases for 0.02 nm at 40 GPa [24]. The pressure of 0.06 GPa would lead to the decrease of interplanar distance of 0.00003 nm. It is only about 3% of the observed shift. In other words, the main input into the shift of the Ag(111) peak gives Cu addition.

However, the instrumental resolution estimated via the standard calibration method with LaB_6 single crystals is such, $\Delta\theta_I \approx 0.08°$, that this shift cannot be credibly interpreted. Moreover, no accurate estimation can be made of the diameter of precipitates in the absence of well-resolved higher order reflections in the XRD spectrum. However, Ag(111) reflections in the as-cast samples before deformation and in homogenized samples after deformation have comparable widths, which is reasonable attributing to precipitates in both samples having comparable diameters on average, $D \approx 33$ nm (Table 1b). It means that HPT destroyed the original coherent Ag flat platelets and led to the formation of extremely tiny new Ag precipitates. The total amount of silver in Ag flat platelets in homogenized before HPT was very low (below 0.1 at.% Ag). The new Ag precipitates contain totally around 1 at.% Ag.

In the *as-cast samples after HPT*, the observed increase of the solute fraction in the matrix after deformation takes place at the expense of pre-existing precipitates. The size of Ag precipitates (determined by XRD) decreased from 33 ± 1 nm to about 12 ± 3 nm.

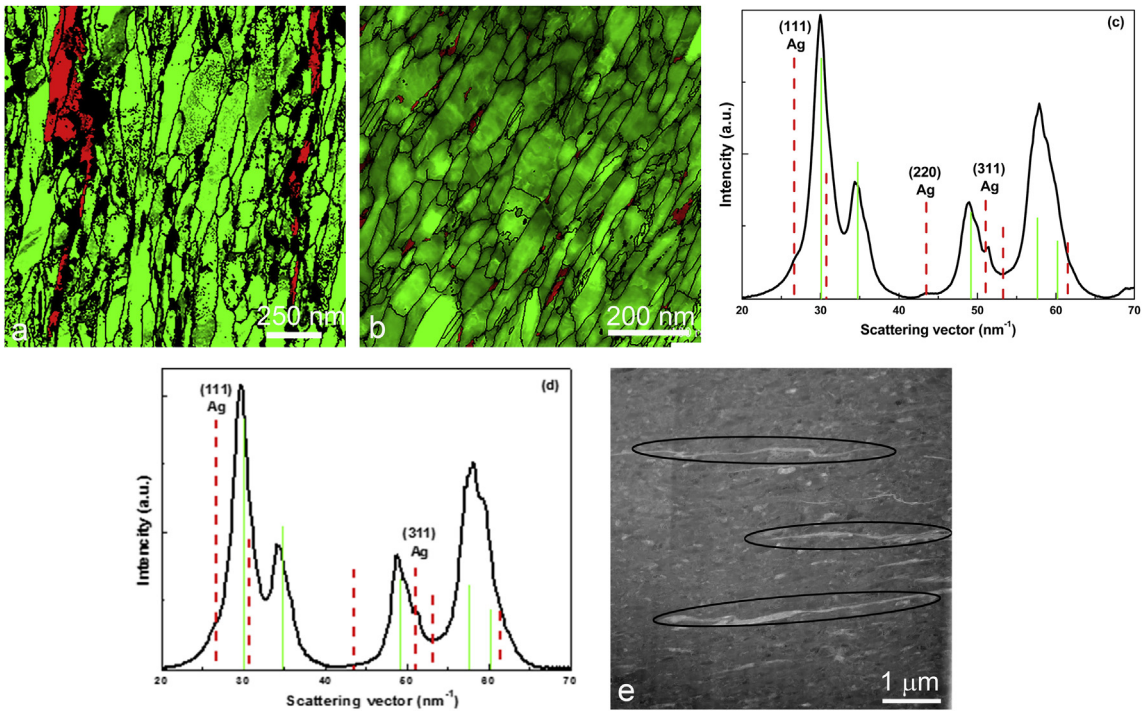

Fig. 4. ACOM-TEM phase maps overlaid with grain boundaries and reliability index (a, b), STEM HAADF micrographs (e) and Selected Area Electron Diffraction (SAED) patterns (c, d) for the homogenized (a, c) and as-cast (b, d, e) samples after HPT. In (a, c) Cu grains are indicated by green and Ag grains are indicated by red color. Solid vertical lines in SAED patterns mark the positions of Cu peaks. Dashed vertical lines mark the Ag peaks.

Alike the case of deformed homogenized samples, a single peak is visible in XRD namely the Ag(111) reflection shifted toward higher diffraction angles with respect to the reference spectrum of pure Ag by, $\Delta\theta \approx 0.208^{\circ}$, thus suggesting that the precipitates contain some diluted copper. In addition, the size of precipitates seems decreasing during HPT since the width of this XRD reflection increases with increasing the deformation. The ACOM-TEM phase map (Fig. 4b) and TEM SAED (Fig. 4d) also prove the presence of the Ag precipitates in the structure. The plot in Fig. 4d represents the results of the SAED pattern digitizing. Intensity maxima for (111) and (311) Ag reflections are observed. Finally, TEM observations show that in deformed 'as-cast' samples small precipitates coexist with large (about 300 × 35 nm^2), foil-shaped silver grains (Fig. 4e).

3.2.2. Grain size in the Cu matrix

Among microstructural changes observed in the samples deformed by SPD/HPT is the grain size refinement in the matrix. This is a widely recognized feature of this type of deformation illustrated by several works in the literature e.g. in Cu and Cu-based alloys [6,25–29]. The same trend is observed in the present work, the initial micrometer grain size decreasing down the nanometer scale during HPT. Tables 1a and 1b summarizes grain size values determined prior and after deformation whereas this trend is confirmed by TEM after HPT (Fig. 4a and c). In addition, the high contrast observed between adjacent grains (Fig. 4a) attests for little intra-granular lattice curvature. Grain diameters displayed in Tables 1a and 1b show that XRD and TEM evaluations differ significantly. Values obtained from dark-field imaging in TEM are larger than XRD estimations based on the modified Williamson-Hall method [8]. However, such differences are expected since XRD is sensitive to the extension of coherent scattering regions such as subgrains and grains, thus yielding information reacher and statistically more accurate than TEM. Finally, it has been found that HPT reduces twice more the diameter of Cu grains in as-cast samples than it does in homogenized ones (Table 1b). This indicates that in as-cast samples, the distance between active shear bands and the spacing and diameters of pre-existing precipitates are on average comparable, a configuration that is reached in homogenized samples only at the late stages of precipitate growth.

3.2.3. Lattice microstrain

The average microstrain of crystal lattice has been estimated from the width at half maxima (F) or from the integral broadening (B) of XRD peaks by using the Williamson-Hall method [8]. The microstrain values collected from deformed homogenized and as-cast samples are comparable yet significantly larger the values found prior to deformation (Table 1b). However, the dispersion of the data is large thus hindering interpretation without additional experiments.

3.2.4. Lattice parameter

Analysis of the whole XRD pattern determines the lattice spacing as an important parameter for the studies of solid solutions. Numerous experimental data achieved for the Cu–Ag system allow one to calculate the silver solubility in the Cu-rich solution with a rather high accuracy [30]. For this purpose, Cu–Ag alloys were homogenized at elevated temperatures, subsequently quenched, and then the values of lattice parameter have been measured as a function of composition throughout the region of solid solution [30]. This general approach was used in this work to study homogenized and as-cast states of Cu–3.9 at. % Ag alloy.

With substantial decreasing grain (or crystallite) size both contraction [31–33] and expansion [34,35] of the fcc lattice has been observed. However, noticeable changes in the lattice parameter of fcc metals, such as Ni, Pd and Cu, take place at 50 nm of crystallite size and lower [36,37]. Magnetron sputtering and ball-milling were applied to produce nanocrystalline thin films and

powders, correspondingly. It should be noted that in the case of Cu the difference in lattice parameter of only 0.003–0.004% appears if the crystallite size dropped down to 20–30 nm. HPT processing does not provide such a strong grain refinement decreasing a grain size in copper and Cu-based alloys approximately to 100 nm.

At the same time, processing conditions of the HPT-technique may cause residual macrostress and consequently affect lattice parameter measurements. XRD measurements of pure Cu before and after HPT (Fig. 1b, open diamond and filled diamond) revealed an increase of the lattice parameter equal to 0.00011 ± 0.00001 nm that could be explained by residual stress as well. This difference found to be in a good agreement with the overestimated (as 0.00008 nm) lattice parameter of HPT Pd [38]. In Ref. [38] the synchrotron XRD measurements have been performed to define correction for a residual macrostress induced by HPT. Earlier [39], the absence of the residual macrostress was reported for HPT Cu. The authors of [39] checked the XRD peak shift after different times of electrolysis erosion. In this work, Fig. 1b demonstrates that these deviations in lattice parameter do not influence the pronounced general trend.

4. Modeling

4.1. Objectives

The above-described results and others from the literature allow concluding that microstructures formed under HPT display the following common aspects:

1) Independent from the initial microstructures of samples, final states obtained by HPT differ significantly from those produced via conventional thermo-mechanical treatments weakly departing from equilibrium. This holds for several microstructural parameters such as grain and precipitate sizes and the matrix composition.
2) In presence of the external solicitation, microstructures are often said converging toward stationary states, though quantitative information in the literature is not systematic and is mainly about the fragmentation in nano-grains. In the present work, this microstructural feature has been quantitatively investigated and different solute partitions are found between initial and final states whereas the matrix composition is converging with increasing deformation toward a value initial-state independent.
3) Physical processes driving the microstructural changes operate at two well separated space scales: the mesoscopic scale defined by the average grain size and the average distance between precipitates, in tight connection with active dislocation glide systems and the nanoscopic scale at which diffusion of species is controlling nucleation and the size of precipitates, the composition of the matrix and the rate of convergence to the stationary state.
4) The microstructure evolves faster than the characteristic time of diffusional transformations where concentrations of point defects are fixed by the thermodynamic equilibrium condition.

Bearing in mind that modeling should comply with all the aspects above, the test is made in this work of diffusive mass transport taken as the controlling mechanism of precipitate growth or dissolution during HPT, driving the alloy toward a uniform stationary composition in the matrix as is experimentally found. Other possible no-diffusive contributions to mass transport are not being considered. At a first sight, measurements [40] of tracer diffusivities in pure Ag, Cu and the binary Ag–Cu system and of the interdiffusion coefficient in the last do not support this working hypothesis since diffusion kinetics at RT is incompatible with the observed rates of change of the composition and of precipitate size during HPT. Moreover, the applied pressure of 6 GPa additionally slows down the diffusion as well as GB migration [41–43]. However, Oberdorfer et al. [44,45] and Čížek et al. [28,46] have shown by means of positron lifetime spectroscopy that in several metallic elements HPT produces an extremely high concentration of vacancies. In Cu under HPT, the first have estimated that athermal vacancy concentrations amount up to, $c \approx 4.5 \cdot 10^{-4}$, whereas the last have concluded that defects agglomerate in clusters made of four vacancies on average and attribute their formation to jogged screw dislocations moving under stress. These works extend previous results by Kiritani et al. [47] and Wu et al. [48] establishing that large concentrations of athermal vacancies are produced by SPD.

In this context, the mobility of atoms under HPT is expected to exceed largely its equilibrium value at RT and the hypothesis becomes plausible of enhanced diffusion controlling growth and dissolution of precipitates and driving compositional changes in the alloy matrix. Thus, main ingredients of modeling are defined as follows: (i) in agreement with the experimental observations of thermal decomposition in Ag–Cu [49], it is assumed that Ag precipitates in homogenized samples grow three-dimensional till their average size and mutual distance become comparable to the spacing of active shear bands. It is worth noting that this hypothesis, further commented on in Section 5, greatly simplifies modeling yet does not fit the platelet-shaped precipitates observed in homogenized samples prior to HPT (Section 3.1, Fig. 2a and b), (ii) in as-cast samples shear bands finely divide pre-existing precipitates at a time scale much shorter than that of diffusion driving composition and precipitate size changes, (iii) the hypothesis is made that HPT fixes the concentration of species at the interface between stable nuclei of the second phase (Ag) at the matrix side (Cu) at a value depending on the macroscopic experimental parameters such as the temperature, the anvil rotation speed, the accumulated strain and the nominal composition of the alloy, (iv) it is assumed that experimental samples can be viewed as a uniform stacking of small spherical volume elements of the matrix embedding a single central spherical precipitate and that under HPT no net diffusion fluxes exist between neighboring such elements, (v) the hypothesis is made that Ag precipitates are pure, though present XRD results are in favor of a mixed composition and (vi) vacancy migration is assumed composition independent since values of the migration energies in the pure metals and the alloy are close to each other [50–52].

4.2. The model

In line with the above assumptions, the evolution during HPT of a spherical Ag precipitate of radius, R, embedded in a spherical volume element, Ω, of radius R_Ω, is described by the following coupled differential equations written in spherical coordinates [53]:

$$\frac{\partial c}{\partial t} = D\left[\frac{\partial^2 c}{\partial t^2} + \frac{2}{r}\frac{\partial c}{\partial r}\right] \tag{1}$$

$$\left(c_p - c_l\right)\frac{dR}{dT} = D\left.\frac{\partial c}{\partial r}\right|_R \tag{2}$$

where, D, is the Ag diffusivity in Cu assumed composition independent, $c = c(r, t)$, is the solute concentration at position, r and elapsed time t, and c_p, c_l, represent respectively the compositions of the Ag precipitate and of the matrix at the interface with the precipitate. Moreover, the following initial and boundary conditions are set:

$$\begin{cases} c(r=R,t)=c_I & 0\le t\le\infty \\ c(r,t=0)=c_I m & R<r\le R_\Omega \\ j(R_\Omega,t)=0 & 0\le t\le\infty \end{cases} \quad (3)$$

with, $j(R_\Omega,vt)$, the flux of solute at the frontier of the volume element, Ω.

The growth case ($c_l < c_m$, $R \approx 0$) can be analytically solved whereas such a solution is not currently available for dissolution ($c_l > c_m$), for reasons extensively discussed by Aaron et al. [53] thus not further commented on here. On the other hand, both cases can be numerically studied by integrating discretized versions of Eqs. (1)–(3), with appropriated values of, c_p, c_m, c_l and $R(0)$, the initial radius of the precipitate. A natural choice is, $c_M^{h,.initial} = 3.9\pm0.1$ at.% Ag and $c_M^{ac,.initial} = 1.9\pm0.1$ at.%Ag for the initial matrix compositions in homogenized and as-cast samples, respectively (Cf. Section 3.1, Table 1a) whereas hypothesis (iv) in Section 4.1 implies, $c_p = 1$. The matrix composition is expected converging toward, c_l, which guarantees that in the long time limit the solute flux vanishes at the precipitate-matrix interface and that the size of precipitates becomes stationary [53]. This is also consistent with the experimental finding that the torsion torque saturates after two anvil rotations (Section 2). Accordingly, the values, $c_l^h = 2.9$ at.%Ag and $c_l^{ac} = 3.0$ at.%Ag, have been selected for the solute concentrations during HPT at the matrix-precipitate interface on the matrix side in homogenized and as-cast samples, respectively (Section 3.2, Table 1b).

Known the values of, c_p, c_m and c_n, the initial radius of the representative average precipitate in the spherical volume element of radius, R_Ω, is approximately given by:

$$\frac{R_\Omega}{R_p}=\frac{1}{R_p^*}\approx\left[\frac{c_p-c_n}{c_n-c_m}\right]^{1/3} \quad (4)$$

provided density changes with varying the composition of the matrix and the size of the precipitate are neglected. In this expression, R_p, is the initial radius of the embedded precipitate. It is worth emphasizing here on that interfacial energy and nucleation mechanisms are not considered in this model and that, given their symmetry, constitutive Eqs (1)–(4) apply to precipitates constrained to evolve while keeping spherical. Additional details about the discretization and the numerical solution of the above equations in reduced space and time coordinates are given in the appendix.

5. Modeling results

5.1. Phase separation (homogenized samples)

With the above listed initial and limit conditions, Eqs (1)–(3) are solved numerically in reduced space and time coordinates (see appendix) with initial radius of the precipitate, $R_p^* \approx 0.065$, given by Eq. (4) and c_p, c_l and c_n values as listed in the preceding section and Table 1b. The precipitate radius is found increasing with elapsed time (Fig. 5a, solid line) at the expense of the solute concentration in the matrix simultaneously decreasing (Fig. 5b, solid line). Both, the solute concentration in the matrix and the precipitate radius saturate above, $\delta t^* \approx 6$, reaching stationary values amounting respectively, $c_m(6) \approx c_l$ and $R_p^*(6) \approx 0.217$. This behavior is consistent with the experimental observation that in both samples, homogenized and as-cast, the torsion torque becomes stationary after two anvil rotations whereas solute fractions in the matrix converge toward a practically common value, which strongly suggests the onset of a stationary microstructural state.

In the growth case, the comparison between analytic and numerical solutions [54] of Eqs (1) and (2), provides a stability and accuracy test of the employed numerical integration scheme. Data points in Fig. 6 at reduced elapsed time, $\delta t^* = 0.125$, coincide with the numerical solution (full line) thus confirming the good behavior of the numerical scheme. This comparison has not been further extended to larger elapsed time values as the analytic solutions in Ref. [54] correspond to the solute concentration at the domain boundary maintained constant whereas in this work numerical solutions satisfy instead a zero flux constraint at this boundary. Additional plots in this figure illustrate the slowing down of the precipitate growth upon approaching the matrix composition the value, $c_m = c_l$.

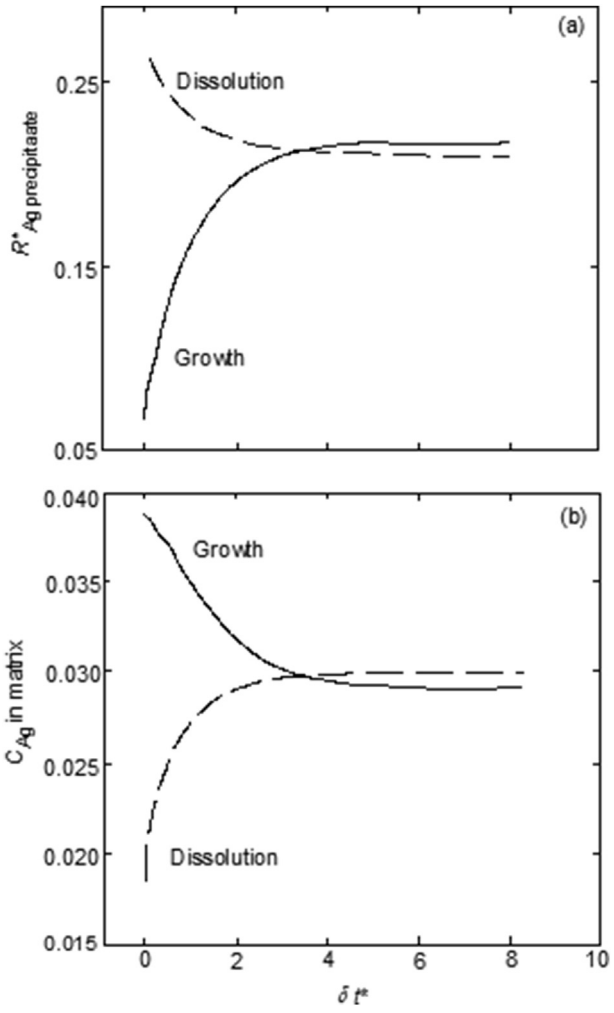

Fig. 5. (a) Diffusive growth and dissolution of precipitates: radii R^* become stationary above elapsed time, $\delta t^* \approx 6$ (reduced units, see appendix). (b) Evolution of Ag-content c_{Ag} in the alloy matrix with elapsed time δt^* (reduced units) during diffusive dissolution (dashed line) or growth (full line) of Ag precipitates. The amount of Ag in solution saturates at elapsed times, $\delta t^* > 6$.

At this stage, modeling and experiments can be tested for consistency by comparing the respective values of the ratio, $\alpha = (R_p^{\text{after HPT}}/R_p^{\text{before HPT}})$, between the precipitate radii after and before HPT. It can be seen in Table 2 that the experimental value, $\alpha_{exp} \approx 3.3$, is in excellent agreement with the modeling prediction, $\alpha_{modeling} \approx 3.32$. This agreement implies that, at fixed nominal composition of the alloy, the evolution of Ag partitioning between precipitates and solute in the matrix is credibly attributed to accelerated diffusion of species during HPT. Indeed, α, is an estimator of the balance between fractions of Ag in precipitates or dissolved in the matrix and of the number density of precipitates, not carrying information about their shapes.

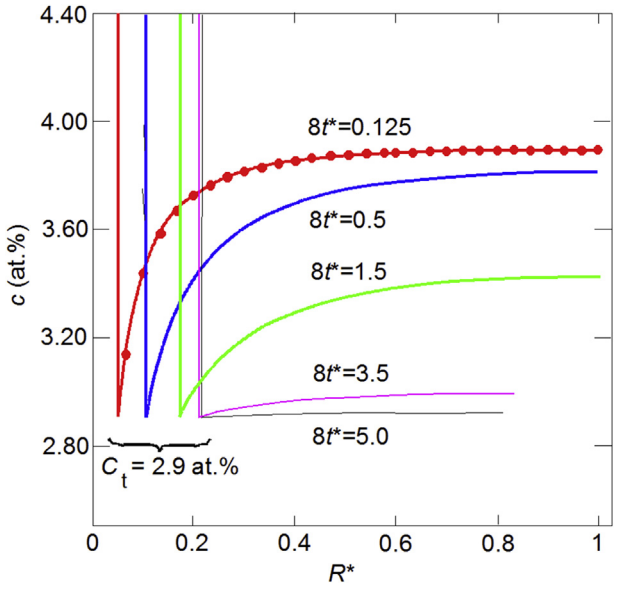

Fig. 6. Diffusive growth of a spherical precipitate: solute (Ag) distribution profiles $c(R^*)$ at selected values of elapsed time δt^*. Full lines: numerical solutions of Eqs. (1)–(3). Full dots represent composition values predicted by the analytical solutions of these equations at $\delta t^* = 0.125$ (see text).

5.2. Partial dissolution of precipitates (as-cast samples)

Inline with the above, the case of the diffusive dissolution of a spherical precipitate can be studied by solving Eqs (1)–(3) with the appropriate boundary and initial conditions. Since no exact analytical solution is available in this case, the equations have been integrated numerically with values, $c_n = 3.9$ at. % Ag, $c_m^{initial} = c_m^{ac} =$ 1.9 at. % Ag and $c_p = 1$ yielding through Eq. (4) the initial radius of the precipitate, $R_p^* \approx 0.27$ and its value after HPT, $R_p^* \approx 0.21$, corresponding to the observed stationary matrix composition, $c_m^{ac} \approx 3$ at. % Ag (Table 1a). Consistently, the numerical solution complies with these reduced radii values as is attested by Fig. 5a (dashed line) and alike in homogeneous samples, the solute distribution and dissolving precipitate radius reach stationary values at reduced elapsed time larger than, $\delta t^* \approx 6$ (Fig. 5a and b, dashed lines). Unlike the case of homogenized samples, the experimental α-ratio is found here about twice larger than the modeling prediction. It is worth noting however that initial distributions of precipitates in homogenized and as-cast samples differ significantly as is shown in Table 1b. In the former, tiny precipitates almost uniformly distributed are less likely affected by shear during HPT than should happen with the much larger in size heterogeneous population seen in the latter (Section 3.2, Tables 1a and b). In the spirit of the remark made in the last paragraph of previous Section 5.1, the agreement between experiment and modeling is recovered by assuming that diffusive dissolution operates on precipitates which average diameter has been reduced by the shear at the very beginning of HPT to half its initial value.

Table 2
Calculated and experimental (in parentheses) values of the ratio, α, between initial (before HPT) and final (after HPT) radii of Ag precipitates and calculated values of the corresponding number densities (after HPT). R_Ω, is the radius of the average spherical element of the alloy embedding a single precipitate, which values have been estimated under the twofold assumption of a uniform distribution of spherical in shape precipitates.

Sample type	$\alpha = (R_p^{\text{after HPT}}/R_p^{\text{before HPT}})$	R_Ω (nm)	10^7 ρ (nm^{-3})
Homogenized	–	76.1	–
Homogenized after HPT	3.32 (3.3)		5.42
As-cast	–	28.8	–
As-cast after HPT	1.3 (2.8)		100

5.3. Real space-time coordinates and modeling

A correspondence can be established between space scales in modeling and experiments by associating the converged precipitate radii in homogenized and as-cast samples, amounting respectively, $R^* = R/R_\Omega \approx 0.217$ and $R^* = R/R_\Omega \approx 0.208$ (Fig. 5a), with half the observed diameters of precipitates after deformation (Table 1b). By doing so, R_Ω in homogenized samples is found ≈ 2.64 times larger its value in the as-cast samples (Table 2). Interestingly, this finding complies with the argument invoked above of shear causing the division of initial precipitates in as-cast samples at the very beginning of HPT. In this context, the evolution of the precipitate distributions in both types of samples via diffusive dissolution or growth should preserve differences in the initial number densities of precipitates persisting till the stationary regime is reached with predicted values listed in Table 2. Unfortunately, experiments cannot help checking the validity of this prediction given the difficulty of statistically meaningful determinations of precipitate densities.

The HPT parameters chosen in this work, namely the applied deformation rate (1 rpm) and the total macroscopic deformation (5 anvil rotations) fix the duration of the HPT essay at, $H_{tot} = 300$ s. On the other hand, since the torsion torque is found saturating after two anvil rotations (Section 3.1) it is reasonable assuming that at elapsed times longer than, $H_s \approx 120$ s, the solute fraction and the size of precipitates have reached stationary values since the mechanical response is tightly correlated with these microstructural ingredients. By analogy, $H_s \approx 120$ s, is assumed corresponding to the elapsed time in modeling above which the solute concentration and the size of precipitates become stationary, $\delta t^* \approx 6$. This fixes the time and mobility scales in modeling, $\tau = 20$ s and $D = R_\Omega^2/\tau \approx 2.9 \cdot 10^{-16}$ m^{2}s^{-1} and provides the basis of comparison with the experiment.

6. Discussion

Binary systems with wide miscibility gap and no intermediate compounds at low and intermediate temperatures are ideally suited for studying phase separation phenomena initiated upon quenching the high-temperature solid solution down to metastable (nucleation and growth) or unstable states (spinodal decomposition). Prepared at near equimolar composition such systems have also been used for studying the microstructures of dynamic states triggered by irradiation [55] or SPD [56–58]. Although SPD-controlled mixing and decomposition have been extensively studied, both experimentally and by means of numerical simulations [58–65], no general consensus has been reached till now about the underlying atomic mechanisms variety of which have been proposed in the literature [63]. However, agreement is now reached about SPD-HPT triggering the formation of large concentrations of athermal vacancies [28,46,64,66].

The present work has been undertaken with the twofold objective of investigating HPT-fashioned microstructures in the model alloy Cu–Ag and for assessing the hypothesis of enhanced diffusive transport of species controlling the formation of dynamic microstructural states. To this end, the alloy has been prepared with different initial microstructures by cooling after solidification (as-cast samples) or water quenching down to RT after long annealing near to the eutectic temperature (homogenized samples). XRD and TEM characterizations have permitted to show that these as-cast and homogenized samples with initially different matrix

compositions and precipitate dimensions evolve under HPT toward practically identical stationary compositions whereas dissolution and growth phenomena lead to stationary yet different average diameters of precipitates.

In parallel, modeling has focused on a volume element of the alloy embedding a pure Ag precipitate with radius and matrix composition representative of the initial states of samples, as determined by XRD and TEM. Diffusion in this model is controlled by the Ag concentration at the interface matrix-precipitate on the matrix side, c_I, a parameter integrating no-equilibrium segregation and other interfacial effects related with the complex microscopic phenomena active during HPT. This phenomenological model with input parameters taken from the experiment has permitted to show that enhanced diffusion in homogenized samples leads to stationary matrix compositions in good agreement with the observations. However, in as-cast samples, the calculated α-ratio between initial and final states has been found twice as large the experimental value. The discrepancy has been attributed to the fragmentation of the precipitates pre-existing in the as-cast samples at the very beginning of HPT, evolving afterwards by diffusion. If realistic, this explanation implies that the average distance between precipitates in as-cast samples before deformation is comparable to the average separation between shear bands in HPT, Λ_s, given by Ref. [67]:

$$\Lambda_S = K\frac{Gb}{\sigma}, \tag{5}$$

where, G, is the Voigt average of the shear elastic moduli of the matrix, b, the Burgers vector of matrix dislocations, σ, the shear stress and K a constant. Thereby, the flow stress in as-cast samples under HPT is estimated by setting, $\Lambda_S = 2R_Q \approx$ 57.6 nm (Table 2), $K = 1$ and by assimilating the matrix to pure Cu i.e. $G \approx 55$ GPa [12] and $b \approx 0.255$ nm at RT, which yields, $\sigma \approx 0.244$ GPa. Being this value consistent with the magnitude of deviatoric stresses acting under HPT, the explanation above sounds credible and further validates the model of diffusive dissolution and growth of precipitates under HPT.

In the present work, non-equilibrium segregation is assumed maintaining constant the solute concentration at the precipitate-matrix interfaces on the matrix side, c_I, which drives the diffusive evolution of precipitates and of the matrix composition. However, without detailed knowledge of the underlying no-equilibrium segregation mechanisms, this key parameter is purely phenomenological, though segregation during HPT has been invoked to explain the formation of stable and uniform Zn-rich layers wetting grain boundaries in Al–Zn alloys [65]. Adding to its phenomenological character, modeling applies to precipitates persisting spherical whereas thin platelets and more complex forms have been observed. However, modeling primarily describes the evolution of the solute in the alloy matrix with input data the concentrations extracted from XRD spectra, which represent the most statistically faithful experimental information. As it has already been commented on, the α-ratio conveniently represents Ag-fractions partitioning between precipitates and solute in the matrix and by no means relates to the shape of precipitates.

This point of the developed model is supported by the fact that the precipitates, indeed, have quite different shape both before and after HPT. Nevertheless, the concentration in the solid solution becomes equal in both samples during the dynamic equilibrium after about two HPT anvil rotations. On the other hand, it has been supposed in the model that each precipitate is active in a certain small volume where the dynamic equilibrium establishes between dissolution and precipitation. The dissolution/precipitation takes place at the interface between precipitate and matrix. It means that precipitates have to be (1) small enough and (2) more or less uniformly distributed in the matrix. We observed in this work that if the solute concentration in both samples is not very different (3.9 and 1.9 at. % Ag), the amount of precipitates is small (almost 0 and 2 at. % Ag, respectively) and the precipitates are fine, then the high pressure torsion form a kind of “attractor” in dynamic equilibrium at 2.9–3.0 at. % Ag in the (Cu) solid solution. The open questions arise, what will happen with this “attractor” if the amount of second phase is high (like in Refs. [56,58,68,69])? What will happen if the precipitates are rough? Is the “attractor” at 2.9–3.0 at. % Ag unique or other “attractors” can also exist (for example, in the Ag-rich solid solutions)? What would happen with the “attractor” concentration of we substitute Ag with other alloying element(s)? These questions have to be answered experimentally and theoretically in the future.

The model gives the following time and mobility scales: $\tau = 20$ s and $D = R_Q^2/\tau \approx 2.9 \cdot 10^{-16}$ m^{2}s^{-1} and, thus, provides the basis of comparison with the experiment. In the model we suppose that the Cu matrix surrounding a precipitate is homogeneous and isotropic. In this case D would correspond to the coefficient of bulk diffusion. The extrapolation of the published results of diffusion measurements to the temperature of the current SPD treatment, T_{SPD}, $T_{SPD} = 300$ K gives $D = 10^{-35}$ m^2/s for self-diffusion in Cu [70] and $D = 10^{-38}$ m^2/s for tracer diffusion of Ag in Cu [71]. The discrepancy of 19 orders of magnitude is hard to explain alone by the (even huge) concentration of athermal vacancies produced by HPT. Already very early it has been observed that the diffusivity in at RT of radiotracer Ag* in nanocrystalline Cu can be quite high $D^{Ag*}_{T=303K} = 3 \cdot 10^{-19}$ m^{2}s^{-1}, and only three orders of magnitude lower then the value in our model [54]. Later it has been realized that copper and copper alloys after SPD (HPT, equal channel angular pressing or surface mechanical attrition) possess a high overall diffusivity [72–74]. The exact analysis demonstrated that the samples after SPD contain the paths of slow and fast diffusion. The extrapolation to RT gives for these paths, respectively, the values of 10^{-18} m^{2}s^{-1} and 10^{-15} m^{2}s^{-1} [74–76]. It is already quite close to the value obtained in our model. Moreover, the point defects produced during SPD (either HPT or ECAP) of initially fully dense coarse grained copper can be accumulated in pores forming the percolating porosity [77–81]. It also increases the overall rate of diffusion penetration through the SPD-treated material. On the other hand, the point defects produced during SPD can form not only the pores but also the percolating network of defects having high diffusivity (mentioned above [74–76]).

We observed that HPT of both samples (as-cast and homogenized) finishes in the equal concentration in (Cu) solid solution. Fig. 1a shows that this concentration corresponds to the solubility limit at $T \approx 680$ °C. The same concentration will be reached if we would anneal both samples (as-cast and homogenized) long enough at $T \approx 680$ °C. In other words, from the viewpoint of composition of (Cu) solid solution the HPT is *equivalent* to anneal at $T \approx 680$ °C.

It happens quite frequently, that the steady-state concentration of a second component in a solid solution after SPD is the same as it would appear in a material after long anneal at a certain (elevated) temperature. This temperature is called effective temperature T_{eff} [4–6,25,26,69]. It has been demonstrated recently that the concept of effective temperature T_{eff} originally proposed by George Martin for the materials under severe irradiation [82] is applicable also for severe plastic deformation (SPD) [6]. If the atomic movements driven by an external action (deformation or irradiation) are higher in comparison with the conventional thermal diffusion, the material is forced to undergo into a state which is equivalent to that at a certain increased (effective) temperature T_{eff}. One can estimate T_{eff}

if the phases in a material after SPD treatment differ from those before SPD (see Fig. 1a and Refs. [6,25,26,41]). The SPD-treatment at ambient temperature T_{SPD} usually leads to the very quick phase transformations, which is easy to understand if one considers the high density of defects, similar to that at the increased temperature. The increased pressure, oppositely, leads to the decrease of diffusivity and/or grain boundary mobility [41–43].

In Ref. [6] we estimated the value of diffusion coefficient which was equivalent to the mass transfer during HPT of Cu–Co alloys at RT. This value was $D = 10^{-16}$ m^2/s. T_{eff} for HPT of Cu–Co alloys was $T_{eff} \approx 900$ °C [6]. The published data on bulk diffusion coefficients give for T_{eff} gives = 900 °C the values of $D = 5{\cdot}10^{-14}$ m^2/s for diffusion of Co in Cu [83] and $D = 10^{-13}$ m^2/s for self-diffusion in Cu [71]. In our case the coefficient for bulk tracer diffusion of Ag in Cu at $T_{eff} \approx 680$ °C is $D = 10^{-15}$ m^2/s [71]. Therefore, the equivalent diffusion coefficient for the SPD-driven mass transfer [6] of the model value obtained in this work (Section 5) is comparable with the conventional diffusion coefficient at (elevated) T_{eff}. This coincidence additionally supports the view point about deep physical links between *equifinal* amount of defects appearing in steady-state during SPD at low temperature T_{SPD} and *equilibrium* defects existing in the same material at elevated temperature T_{eff}.

Another important point is the influence of grain boundaries. SPD leads to the strong grain refinement, also in our case. The specific area of grain boundaries (GBs) increases and the GB adsorption consumes the second component. Though the maximal solubility of a second component in the lattice does not change, its apparent solubility in fine- or nanograined matrix can strongly increase [84]. It is because the thin GB layers do not contribute into XRD patterns, they are thus "invisible" for XRD. If the concentration of a second component is fixed, the grain refinement leads to decrease of the amount of precipitates because second component "disappears" more and more into GB adsorption layers [84,85]. In this work the silver concentration is well above the "attractor" concentration of 2.9–3.0 at. % Ag (see Fig. 1a), the amount of precipitates is high enough, and, therefore, the role of GB adsorption cannot be distinguished. However, basing in the facts observed in this work, we can predict the following scenario. Suppose that we prepare the alloy with Ag content well below the "attractor" of 2.9–3.0 at. % Ag, say, 1 at. % Ag, homogenize it at 600 °C and start to deform with HPT. In this case no precipitates appear because 1 at. % Ag $\ll$ 2.9 at. % Ag (see Fig. 1a). However, the newly formed GBs would need the silver for the GB adsorption layers [86–89]. Since no precipitates are available, the Ag from the (Cu) solid solution would be consumed, and the lattice spacing in (Cu) would decrease (see Fig. 1b). Such an experiment can also be conducted in the future.

7. Conclusions

In summary, the competition (and dynamic equilibrium) between precipitation and dissolution during high pressure torsion (HPT) has been for the first time simultaneously analyzed in experiments and modeling. We observed in experiment that during HPT of a two-phase alloy two simultaneous and competing processes indeed take place, namely (1) the dissolution of precipitates and (2) decomposition of supersaturated solid solution with precipitation of a second phase. As a result, a dynamic equilibrium between these two processes appears, and a certain steady-state concentration in a solid solution is reached. This concentration is equifinal and equivalent to that in the sample annealed at the effective temperature $T_{eff} \approx 680$ °C. The present work has shown that in the studied alloy, HPT triggers the emergence of metastable microstructural states characterized by stationary values of the matrix composition and of the diameters of precipitates. The stationary solute concentration in the matrix has revealed initial-state independent with value well above the equilibrium solubility limit at RT. However, since precipitates transform via partial dissolution or growth with otherwise fixed experimental parameters, their shape, dimension and density still preserve the memory of the initial state. Finally, by assuming that dynamic segregation during HPT maintains constant at a non-equilibrium value the composition at matrix-precipitate interfaces, the experimental findings are found consistent with enhanced diffusion of species controlling the stationary matrix composition and precipitate number densities.

Acknowledgements

The work has been partially supported by the Russian Foundation for Basic Research (grants 14-08-00972 and 15-08-09325), the Russian Federal Ministry for Education and Science (Increase Competitiveness Program of NUST«MISiS»), National Science Centre of Poland (grant OPUS 2014/13/B/ST8/04247), the EraNet.Rus program (grant STProjects-219) and Karlsruhe Nano Micro Facility. Illuminating discussions with G. Baldinozzi, L. Luneville and D. Simeone at CEA/CentraleSupelec LRC-CARMEN are gratefully acknowledged.

APPENDIX

For the sake of convenience Eqs. (2) and (3), are rewritten by using reduced space and time variables as follows:

$$\begin{cases} \dfrac{\partial c}{\partial \tilde{t}} = \dfrac{\partial^2 c}{\partial \tilde{r}^2} + \dfrac{2}{\tilde{r}}\dfrac{\partial c}{\partial \tilde{r}} \\ (c_p - c_t)\dfrac{\partial \tilde{R}}{\partial \tilde{t}} = \left.\dfrac{\partial c}{\partial \tilde{r}}\right|_{\tilde{r}=\tilde{R}} \end{cases} \quad \delta\tilde{t} = \frac{\delta t}{\tau}, \tau = \frac{R_\Omega^2}{D}, \delta\tilde{r} = \frac{\delta r}{R_\Omega}, \tag{A1}$$

where D, represents the diffusivity of Ag in the matrix. Twofold discretization in time and space, leads then to the following finite differences equations:

$$\begin{cases} c(i,j+1) = c(i,j) + \dfrac{\delta\tilde{t}}{\delta\tilde{r}^2}[c(i+1,j) + c(i-1,j) - 2c(i,j)] + \dfrac{\delta\tilde{t}}{\delta\tilde{r}^2}\dfrac{1}{r_t^*}[c(i+1,j) + c(i-1,j) - 2c(i,j)] \\ R_{j+1}^* = R_j^* + \dfrac{\delta\tilde{t}}{\delta\tilde{r}^2}\left[\dfrac{c(i+1,j) - c(i,j)}{c_p - c_i}\right] \end{cases}, \tag{A2}$$

where $r_l^* = \dfrac{\tilde{r}_i}{\delta\tilde{r}}, R_j^* = \dfrac{\tilde{R}_j}{\delta\tilde{r}}$,

where, i and j, represent respectively discrete space and time coordinates. The evolution of a precipitate submitted to various initial and boundary conditions has been obtained from Eq. (A2) integrated up to elapsed time, $\delta t = 10\tau$ in the domain, $[0, R_\Omega]$, with space discretization step, $\delta r^* = 1/600 \approx 1.667\ 10^{-3}$. It is worth noting that this simple explicit scheme is conditionally stable [90], in the interval, $\delta\tilde{t}/\delta\tilde{r}^2 \in [0, 0.5]$ and that in the present work this ratio values has been set equal to the upper limit of the stability interval.

References

[1] R.Z. Valiev, R.K. Islamgaliev, I.V. Alexandrov, Bulk nanostructured materials from severe plastic deformation, Prog. Mater. Sci. 45 (2000) 103–189.
[2] E.I. Teitel', L.S. Metlov, D.V. Gunderov, A.V. Korznikov, On the structural and phase transformations in solids induced by severe plastic deformation, Phys. Metall. Metallogr. 113 (2012) 1162–1168.
[3] X. Sauvage, A. Chbihi, X. Quelennec, Severe plastic deformation and phase transformations, J. Phys. 240 (2010) 012003.
[4] B. Straumal, A. Korneva, P. Zięba, Phase transitions in metallic alloys driven by the high pressure torsion, Arch. Civ. Mech. Eng. 14 (2014) 242–249.
[5] B.B. Straumal, A.R. Kilmametov, Yu. Ivanisenko, A.A. Mazilkin, O.A. Kogtenkova, L. Kurmanaeva, A. Korneva, P. Zięba, B. Baretzky, Phase transitions induced by severe plastic deformation: steady-state and equifinality, Int. J. Mater. Res. 106 (2015) 657–664.
[6] B.B. Straumal, A.R. Kilmametov, Yu.O. Kucheev, L. Kurmanaeva, Yu. Ivanisenko, B. Baretzky, A. Korneva, P. Zięba, D.A. Molodov, Phase transitions during high pressure torsion of Cu-Co alloys, Mater. Lett. 118 (2014) 111–114.
[7] T.B. Massalski (Ed.), Binary Alloy Phase Diagrams, ASM International, Materials Park, Ohio, USA, 1990.
[8] A. Kobler, A. Kashiwar, H. Hahn, C. Kübel, Combination of in situ straining and ACOM TEM: a novel method for analysis of plastic deformation of nanocrystalline metals, Ultramicroscopy 128 (2013) 68–81.
[9] J. Markmann, V. Yamakov, J. Weissmueller, Validating grain size analysis from X-ray line broadening: a virtual Experiment, Scr. Mater. 59 (2008) 15–18.
[10] M. Wojdyr, Fityk: a general-purpose peak fitting program, J. Appl. Cryst. 43 (2010) 1126–1128.
[11] E. Schmid, G. Siebel, Über die Mischkristallbildung bei ein- und vielkristallinem Material, Z. Phys. 85 (1932) 36–55.
[12] G. Simmons, H. Wang, Single Crystal Elastic Constants and Calculated Aggregate Properties: a Handbook, The M.I.T Press, Cambridge, 1971.
[13] N. Ageew, M. Hansen, G. Sachs, Entmischung und Eigenschaftänderungen übersättigter Silber-Kupferlegierungen, Z. Angew. Phys. 66 (1930) 350–376.
[14] H.D. Megaw, Lattice dimensions in copper-silver alloys, Philos. Mag. 14 (1932) 130–142.
[15] E.A. Owen, J. Rogers, X-ray study of copper-silver alloys, J. Inst. Met. 57 (1935) 257–266.
[16] A. Guinier, Structure of age-hardened aluminium-copper alloys, Nature 142 (1938) 569–570.
[17] G.D. Preston, Structure of age-hardened aluminium-copper alloys, Nature 142 (1938), 570–570.
[18] I. Konyashin, F. Lachmann, B. Ries, A.A. Mazilkin, B.B. Straumal, Chr. Kübel, L. Llanes, B. Baretzky, Strengthening zones in the Co matrix of WC-Co cemented carbides, Scr. Mater. 83 (2014) 17–20.
[19] A.A. Mazilkin, B.B. Straumal, M.V. Borodachenkova, R.Z. Valiev, O.A. Kogtenkova, B. Baretzky, Gradual softening of Al–Zn alloys during high-pressure torsion, Mater. Lett. 84 (2012) 63–65.
[20] J.M. Howe, Interfaces in Materials: Atomic Structure, Thermodynamics and Kinetics of Solid-vapor, Solid-liquid and Solid-solid Interfaces, John Wiley & Sons, New York, 1997.
[21] E. Murr, Interfacial Phenomena in Metals and Alloys, Addison Wesley, Reading MA, 1975.
[22] J. Schölhammer, B. Baretzky, W. Gust, E. Mittemeijer, B. Straumal, Grain boundary grooving as an indicator of grain boundary phase transformations, Interf. Sci. 9 (2001) 43–53.
[23] B.B. Straumal, S.A. Polyakov, E.J. Mittemeijer, Temperature influence on the faceting of Σ3 and Σ9 grain boundaries in Cu, Acta Mater. 54 (2006) 167–172.
[24] E.A. Grumman-Petrushka, High Pressure Studies of Nanocrystalline Silver, Nanocrystalline Silicon Carbide, and Bulk Zirconium Pyrophosphate, M.Sc. Thesis of University of Exeter, UK, 1987, Kansas City, Missouri, 2008.
[25] B.B. Straumal, A.A. Mazilkin, B. Baretzky, E. Rabkin, R.Z. Valiev, Accelerated diffusion and phase transformations in Co-Cu alloys driven by the severe plastic deformation, Mater. Trans. 53 (2012) 63–71.
[26] B.B. Straumal, S.G. Protasova, A.A. Mazilkin, E. Rabkin, D. Goll, G. Schütz, B. Baretzky, R. Valiev, Deformation-driven formation of equilibrium phases in the Cu-Ni alloys, J. Mater. Sci. 47 (2012) 360–367.
[27] N. Lugo, N. Llorca, J.M. Cabrera, Z. Horita, Microstructures and mechanical properties of pure copper deformed severely by equal-channel angular pressing and high pressure torsion, Mater. Sci. Eng. A 477 (2008) 366–371.
[28] J. Čížek, M. Janeček, O. Srba, R. Kužel, Z. Barnovská, I. Procházka, S. Dobatkin, Evolution of defects in copper deformed by high-pressure torsion, Acta Mater. 59 (2011) 2322–2329.
[29] X.Z. Liao, Y.H. Zhao, Y.T. Zhu, R.Z. Valiev, D.V. Gunderov, Grain-size effect on the deformation mechanisms of nanostructured copper processed by high-pressure torsion, J. Appl. Phys. 96 (2004) 636–640.
[30] P.R. Subramanian, J.H. Perepezko, The Ag-Cu (Silver-Copper) system, J. Phase Equilibria 14 (1993) 62–75.
[31] G. Apai, J.F. Hamilton, J. Stohr, A. Thompson, Extended X-ray—absorption fine structure of small Cu and Ni clusters: binding-energy and bond-length changes with cluster size, Phys. Rev. Lett. 43 (1979) 165–168.
[32] C.W. Mays, J.S. Vermaak, D. Kuhlmann-Wilsdorf, On surface stress and surface tension: II. Determination of the surface stress of gold, Surf. Sci. 12 (1968) 134–140.
[33] X.F. Yu, X. Liu, K. Zhang, Z.Q. Hu, The lattice contraction of nanometer-sized Sn and Bi particles produced by an electrohydrodynamic technique, J. Phys. Condens. Matter 11 (1999) 937–944.
[34] P.P. Chatterjee, S.K. Pabi, I. Manna, An allotropic transformation induced by mechanical alloying, J. Appl. Phys. 86 (1999) 5912–5926.
[35] Z.M. Wang, J.Y. Wang, L.P.H. Jeurgens, F. Phillipp, E.J. Mittemeijer, Origins of stress development during metal-induced crystallization and layer exchange: annealing amorphous Ge/crystalline Al bilayers, Acta Mater. 56 (2008) 5047–5057.
[36] J. Sheng, U. Welzel, E.J. Mittemeijer, Nonmonotonic crystallite-size dependence of the lattice parameter of nanocrystalline nickel, Appl. Phys. Lett. 97 (2010) 153109.
[37] G.K. Rane, U. Welzel, S.R. Meka, E.J. Mittemeijer, Non-monotonic lattice parameter variation with crystallite size in nanocrystalline solids, Acta Mater. 61 (2013) 4524–4533.
[38] L. Kurmanaeva, Y. Ivanisenko, J. Markmann, Grain refinement and mechanical properties in ultrafine-grained Pd and Pd–Ag alloys produced by HPT, Mater. Sci. Eng. A 527 (2010) 1776–1783.
[39] K. Zhang, I.V. Alexandrov, R.Z. Valiev, K. Lu, Structural characterization of nanocrystalline copper by means of X-ray diffraction, J. Appl. Phys. 80 (1996) 5617–5624.
[40] D.B. Butrymowicz, J.R. Manning, M.E. Read, Diffusion in copper and copper alloys, Part II. Copper–silver and copper–gold systems, J. Phys. Chem. Ref. Data 3 (1974) 527–602.
[41] B.B. Straumal, L.M. Klinger, L.S. Shvindlerman, The influence of pressure on indium diffusion along single tin-germanium interphase boundaries, Scr. Metall. 17 (1983) 275–279.
[42] D.A. Molodov, B.B. Straumal, L.S. Shvindlerman, The effect of pressure on migration of ⟨001⟩ tilt grain boundaries in tin bicrystals, Scr. Metall. 18 (1984) 207–211.
[43] D.A. Molodov, J. Swiderski, G. Gottstein, W. Lojkowski, L.S. Shvindlerman, Effect of pressure on grain boundary migration in aluminium bicrystals, Acta Metall. Mater. 42 (1994) 3397–3407.
[44] B. Oberdorfer, E.-M. Steyskal, W. Sprengel, W. Puff, M. Zehetbauer, R. Pippan, R. Wuerschum, In situ probing of fast defect annealing in Cu and Ni with a high-intensity positron beam, Phys. Rev. Lett. 105 (2010) 146101.
[45] B. Oberdorfer, D. Setman, E.-M. Steyskal, A. Hohenwarter, W. Sprengel, M. Zehetbauer, R. Pippan, R. Würschum, Grain boundary excess volume and defect annealing of copper after high-pressure torsion, Acta Mater 68 (2014) 189–195.
[46] J. Čížek, O. Melikhova, Z. Barnovská, I. Procházka, R.K. Islamgaliev, Vacancy clusters in ultra fine grained metals prepared by severe plastic deformation, J. Phys. Conf. Ser. 443 (2013) 012008.
[47] M. Kiritani, Y. Satoh, Y. Kizuka, K. Arakawa, Y. Ogasawara, S. Arai, Y. Shimomura, Anomalous production of vacancy clusters and the possibility of plastic deformation of crystalline metals without dislocations, Philos. Mag. Lett. 79 (1999) 797–804.
[48] X.L. Wu, B. Li, E. Ma, Vacancy clusters in ultrafine grained Al by severe plastic deformation, J. Appl. Phys. Lett. 91 (2007) 141908.
[49] K. Labisz, Z. Rdzawski, M. Pawlyta, Microstructure evaluation of long-term aged binary Ag-Cu alloy, Arch. Mater. Sci. Eng. 49 (2011) 15–24.
[50] R.R. Bourassa, B. Lengeler, The formation and migration energies of vacancies in quenched copper, J. Phys. F. Met. Phys. 6 (1976) 1405–1413.
[51] R.W. Balluffi, Vacancy defect mobilities and binding energies obtained from annealing studies, J. Nucl. Mater. 69–70 (1978) 240–263.
[52] J. Hillairet, C. Mairy, C. Minier, P. Hautojärvi, A. Vehanen, J. Yli-Kaupilla, Assignment of radiation-enhanced ordering to vacancies and self-interstitials in alpha-AgZn alloys, in: J. Takamura, M. Doyama, M. Kiritani (Eds.), Point Defects and Defect Interactions in Metals (Yamada Conference V), Tokyo press, Japan, 1982, pp. 284–288.
[53] H.B. Aaron, D. Fainstein, G.R. Kotler, Diffusion-Limited Phase Transformations: a comparison and critical evaluation of the mathematical approximations, J. Appl. Phys. 41 (1970) 4404–4410.
[54] S. Schumacher, R. Birringer, R. Straub, H. Gleiter, Diffusion of silver in nanocrystalline copper between 303 and 373 K, Acta Metall. 37 (1989) 2485–2488.
[55] L. Luneville, G. Demange, V. Pontikis, D. Simeone, Phase-field modelling of radiation induced microstructures, Mater. Res. Soc. Symp. Proc. (2015) 1743–1748.
[56] S.N. Arshad, T.G. Lach, M. Pouryazdan, H. Hahn, P. Bellon, S.J. Dillon, R.S. Averback, Dependence of shear-induced mixing on length scale, Scr. Mater. 68 (2013) 215–218.
[57] E.H. Ekiz, T.G. Lach, R.S. Averback, N.A. Mara, I.J. Beyerlein, M. Pouryazdan, H. Hahn, P. Bellon, Microstructural evolution of nanolayered Cu-Nb

composites subjected to high-pressure torsion, Acta Mater. 72 (2014) 178–191.
[58] M. Pouryazdan, D. Schwen, D. Wang, T. Scherer, H. Hahn, R.S. Averback, P. Bellon, Forced chemical mixing of immiscible Ag-Cu heterointerfaces using high-pressure torsion, Phys. Rev. B 86 (2012) 144302.
[59] P. Bellon, R.S. Averback, Nonequilibrium roughening of interfaces in crystals under shear: application to ball milling, Phys. Rev. Lett. 74 (1995) 1819–1822.
[60] S. Shu, P. Bellon, R.S. Averback, Complex nanoprecipitate structures induced by irradiation in immiscible alloy systems, Phys. Rev. B 87 (2013) 144102.
[61] Y. Ashkenazy, N.Q. Vo, D. Schwen, R.S. Averback, P. Bellon, Shear induced chemical mixing in heterogeneous systems, Acta Mater. 60 (2012) 984–993.
[62] F. Wu, P. Bellon, A.J. Melmed, T.A. Lusby, Forced mixing and nanoscale decomposition in ball-milled Cu-Ag characterized by APFIM, Acta Mater. 49 (2001) 453–461.
[63] D. Raabe, S. Ohsaki, K. Hono, Mechanical alloying and amorphization in Cu–Nb–Ag in situ composite wires studied by transmission electron microscopy and atom probe tomography, Acta Mater. 57 (2009) 5254–5263.
[64] S.N. Arshad, T.G. Lach, J. Ivanisenko, D. Setman, P. Bellon, S.J. Dillon, R.S. Averback, Self-organization of Cu–Ag during controlled severe plastic deformation at high temperatures, J. Mater. Res. 30 (2015) 1943–1956.
[65] B.B. Straumal, X. Sauvage, B. Baretzky, A.A. Mazilkin, R.Z. Valiev, Grain boundary films in Al–Zn alloys after high pressure torsion, Scr. Mater. 70 (2014) 59–62.
[66] S.V. Divinski, J. Ribbe, D. Baither, G. Schmitz, G. Reglitz, H. Rösner, K. Sato, Y. Estrin, G. Wilde, Nano- and micro-scale free volume in ultrafine grained Cu–1 wt.% Pb alloy deformed by equal channel angular pressing, Acta Mater. 57 (2009) 5706–5717.
[67] J. Friedel, Dislocations, Pergamon Press, New York, 1964.
[68] F. Ren, S.N. Arshad, P. Bellon, R.S. Averback, M. Pouryazdan, H. Hahn, Sliding wear-induced chemical nanolayering in Cu–Ag, and its implications for high wear resistance, Acta Mater. 72 (2014) 148–158.
[69] A. Korneva, B. Straumal, R. Chulist, A. Kilmametov, P. Bała, G. Cios, N. Schell, P. Zięba, Grain refinement of intermetallic compounds in the Cu–Sn system under high pressure torsion, Mater. Lett. 179 (2016) 12–15.
[70] S. Fujikawa, K.I. Hirano, Bulk self diffusion in copper, in: J.I. Takamura, M. Doyama, M. Kiritani (Eds.), Proc. Of Yamada Vth Conf. on Point Defects, Defect Interactions in Metals, Univ. of Tokyo Press, Tokyo, 1982, pp. 554–558.
[71] H. Mehrer (Ed.), Diffusion in Solid Metals and Alloys, Landolt-börnstein New Series, Gr III, vol. 26, Springer-Verlag, Berlin, 1990, p. 187.
[72] Z.B. Wang, K. Lu, G. Wilde, S.V. Divinski, Interfacial diffusion in Cu with a gradient nanostructured surface layer, Acta Mater. 58 (2010) 2376–2386.
[73] Z.B. Wang, K. Lu, G. Wilde, S. Divinski, Toward the existence of ultrafast diffusion paths in Cu with a gradient microstructure: room temperature diffusion of Ni, Appl. Phys. Lett. 93 (2008) 131904.
[74] Y. Amouyal, S.V. Divinski, Y. Estrin, E. Rabkin, Short-circuit diffusion in an ultrafine-grained copper–zirconium alloy produced by equal channel angular pressing, Acta Mater. 55 (2007) 5968–5979.
[75] M. Wegner, J. Leuthold, M. Peterlechner, X. Song, S.V. Divinski, G. Wilde, Grain boundary and triple junction diffusion in nanocrystalline copper, J. Appl. Phys. 116 (2014) 093514.
[76] Y. Amouyal, S.V. Divinski, L. Klinger, E. Rabkin, Grain boundary diffusion and recrystallization in ultrafine grain copper produced by equal channel angular pressing, Acta Mater. 56 (2008) 5500–5513.
[77] M. Wegner, J. Leuthold, M. Peterlechner, D. Setman, M. Zehetbauer, R. Pippan, S.V. Divinski, G. Wilde, Percolating porosity in ultrafine grained copper processed by High Pressure Torsion, J. Appl. Phys. 114 (2013) 183509.
[78] J. Ribbe, G. Schmitz, D. Gunderov, Y. Estrin, Y. Amouyal, G. Wilde, S.V. Divinski, Effect of annealing on percolating porosity in ultrafine-grained copper produced by equal channel angular pressing, Acta Mater. 61 (2013) 5477–5486.
[79] J. Ribbe, G. Schmitz, H. Rösner, R. Lapovok, Y. Estrin, G. Wilde, S.V. Divinski, Effect of back pressure during equal-channel angular pressing on deformation-induced porosity in copper, Scr. Mater. 68 (2013) 925–928.
[80] S.V. Divinski, J. Ribbe, G. Reglitz, Y. Estrin, G. Wilde, Percolating network of ultrafast transport channels in severely deformed nanocrystalline metals, J. Appl. Phys. 106 (2009) 063502.
[81] J. Ribbe, D. Baither, G. Schmitz, S.V. Divinski, Ultrafast diffusion and internal porosity in ultrafine-grained copper–lead alloy prepared by equal channel angular pressing, Scr. Mater. 61 (2009) 129–132.
[82] G. Martin, Phase stability under irradiation: ballistic effects, Phys. Rev. B 30 (1984) 1424–1436.
[83] C.A. Mackliet, Diffusion of iron, cobalt, and nickel in single crystals of pure copper, Phys. Rev. 109 (1958) 1964–1970.
[84] B.B. Straumal, A.A. Mazilkin, S.G. Protasova, A.A. Myatiev, P.B. Straumal, B. Baretzky, Increase of Co solubility with decreasing grain size in ZnO, Acta Mater. 56 (2008) 6246–6256.
[85] B.B. Straumal, S.V. Dobatkin, A.O. Rodin, S.G. Protasova, A.A. Mazilkin, D. Goll, B. Baretzky, Structure and properties of nanograined Fe–C alloys after severe plastic deformation, Adv. Eng. Mater. 13 (2011) 463–469.
[86] T. Frolov, S.V. Divinski, M. Asta, Y. Mishin, Effect of interface phase transformations on diffusion and segregation in high-angle grain boundaries, Phys. Rev. Lett. 110 (2013) 255502.
[87] S.V. Divinski, H. Edelhoff, S. Prokofjev, Diffusion and segregation of silver in copper Σ5(310) grain boundary, Phys. Rev. B 85 (2012) 144104.
[88] H. Edelhoff, S.I. Prokofjev, S.V. Divinski, The C-regime measurements of grain boundary diffusion of silver in copper Σ5(310) bicrystal, Scr. Mater. 64 (2011) 374–377.
[89] S.V. Divinski, J. Ribbe, G. Schmitz, C. Herzig, Grain boundary diffusion and segregation of Ni in Cu, Acta Mater. 55 (2007) 3337–3346.
[90] D.A. Tavella, Quantitative Methods in Derivatives Pricing : an Introduction to Computational Finance, J. Wiley & Sons, Inc., New York, 2002, ISBN 978-0-471-39447-1.